MANGO: An optical network to study the dynamics of the Earth's upper atmosphere

A. N. Bhatt[1], B. J. Harding[2], J. J. Makela[3], L. Navarro[4], L. Lamarche[1], T. Valentic[1], E. A. Kendall[5], P. Venkatraman[3]

[1]Center for Geospace Studies, SRI International, Menlo Park, California
[2]Department of Electrical and Computer Engineering, University of Illinois Urbana-Champaign, Urbana, Illinois
[3]University of California, Berkeley, California
[4]University of Colorado Boulder, Boulder, Colorado

Key Points:

- A network of red and green line cameras and Fabry-Perot interferometers is being developed in mid-latitude USA
- The network observes dynamics in two altitude regions of the upper atmosphere
- The data are used to understand the upper atmospheric response to energetic events generated in the lower atmosphere or the sun

Corresponding author: Asti Bhatt, asti.bhatt@sri.com

Abstract

The Mid-latitude All-sky-imaging Network for Geophysical Observations (MANGO) employs a combination of two powerful optical techniques used to observe the dynamics of Earth's upper atmosphere: wide-field imaging and high-resolution spectral interferometry. Both techniques observe the naturally occurring airglow emissions produced in the upper atmosphere at 630.0- and 557.7-nm wavelengths. Instruments are deployed to sites across the continental United States, providing the capability to make measurements spanning mid to sub-auroral latitudes. The current instrument suite in MANGO has five all-sky imagers observing the 630.0-nm emission (integrated between 250-400 km altitude), four all-sky imagers observing the 557.7-nm emission (integrated between 97-100 km altitude), and three Fabry-Perot interferometers measuring neutral winds and temperature using both these wavelengths. The deployment of additional imagers is planned. The network makes unprecedented observations of the nighttime thermosphere-ionosphere dynamics with the expanded field-of-view provided by the distributed network of instruments. This paper describes the network, the instruments, the data products, and first results from this effort.

1 Introduction

The Earth's ionosphere serves as an interaction region between plasma and neutral dynamics. The lower atmosphere drives wave processes that transfer energy and momentum to the ionosphere. The magnetosphere in turn drives high-energy events during geomagnetically active times, producing global changes in the ionospheric composition and drift. The National Research Council Decadal Survey [2012] noted that these coupling processes at varying scales in space and time are still poorly understood as they involve a host of multiscale dynamics. As a result, a key science challenge of this decade is to "determine the dynamics and coupling of Earth's magnetosphere, ionosphere, and atmosphere and their response to solar and terrestrial inputs."

Progress in addressing this challenge has traditionally been difficult due to the complexity of coupled multi-scale processes and the vastness of the geospace system. While the global whole-atmosphere models have been able to represent the variability of this coupled system in a statistical sense, the ability to reproduce or validate the instantaneous or small-scale dynamics is missing, due to unavailability of key measurements of geophysical parameters characterizing plasma and neutral dynamics at various scales. Much about the neutral dynamics has been learned by measuring atomic oxygen as it is a dominant species in the thermosphere. However, historically the measurements have been conducted by stand-alone instruments and the large-scale system dynamics are not captured.

For decades, measurements of low-brightness nightglow emissions resulting from dissociative recombination of molecular oxygen have been carried out from stand-alone locations [e.g., Taylor (1997); Mendillo et al. (1997); Garcia et al. (2000)]. While these initiatives gave us insights into the brighter and more commonly observed phenomena (e.g., aurorally generated large-scale travelling ionospheric disturbances [LSTIDs] – e.g., Kubota et al. (2001); southwestward propagating medium-scale TIDs [MSTIDs] – e.g., Martinis et al. (2010), the limited fields-of-view hampered our ability to understand the generation, propagation, and dissipation conditions needed by these traveling structures.

In recent years, the geospace community has realized the usefulness of distributed arrays of identical instruments for making multi-scale measurements across vast geographic scales [e.g., THEMIS: Mende et al. (2007); GPS TEC network: Tsugawa et al. (2007); All-sky imaging and TEC: Lyons et al. (2019); SuperDARN: Nishitani et al. (2019)]. Optical instruments like all-sky imagers (ASIs) and Fabry-Perot interferometers (FPIs) that observe emissions and thereby dynamics from a specific altitude region play a critical role in addressing the coupling question. The ionosphere-thermosphere (IT) system is

driven by energy and momentum transfer, and atomic oxygen density variations imposed, from both the magnetosphere and the lower atmosphere. In general, these have been treated as independent from each other, yet the interactions between all the components can often lead to emergent behavior. At high latitudes, active periods see a complex set of changes involving particle precipitation and electric fields, which makes it very difficult to distinguish these two drivers. The mid-latitudes provide an ideal environment for understanding the impact of lower atmospheric forcing on the IT system because this region is usually less disturbed by geomagnetic activity than higher latitudes allowing observations of airglow in the absence of complicating auroral dynamics.

At mid-latitudes, the MANGO network was established with a goal to broaden the FOV of 630.0-nm (red-line) airglow observations to cover several latitude/longitude sectors and enable identification of potential sources of mid-latitude medium and large-scale waves. The measurements from over three years of MANGO's operations suggest the following: 1. The structures/waves in the mid-latitude O(^{1}D) 630.0-nm airglow are observed to be propagating in multiple directions in addition to the widely reported southwestward-propagating MSTIDs that match with GPS TEC variations; 2. Waves/structures from high-latitude drivers and those likely generated from lower atmospheric sources interact at mid-latitudes, resulting in emergent behavior.

However, these initial MANGO results did not include knowledge of an underlying thermospheric state that is critical to determine the vertical wavelength and that affects the upward propagation of gravity waves. As a result, while we have gained new understanding of dynamic plasma structuring in the mid-latitudes during geomagnetically quiet and active conditions, and have educated speculation about sources of observed disturbances (Lyons et al., 2019), we know little about the enabling circumstances for propagation of these disturbances/waves.

Thermospheric wind and neutral temperature observations have been conducted for many decades from individual ground-based FPIs. This historical database has provided excellent information on the temporal evolution of the winds at a single location, which has informed climatological models such as the Horizontal Wind Model (Drob et al., 2015). Recently, FPIs and other wind-measuring instruments have been deployed in networks, allowing for the study of meso- and small-scale structures in the thermospheric wind field [e.g., Navarro and Fejer (2019), Makela et al. (2012), Harding et al. (2015)]

Starting in 2021, MANGO underwent a second phase of expansion. Here, we report on initial results from the expanded MANGO network, which now includes four FPIs in addition to thirteen imaging systems, operating as a single coordinated distributed array. After describing the network, instruments, and data products, we present key first results that demonstrate the strengths of the combined imaging and FPI observations in studying the dynamics of this region of the upper atmosphere.

2 The Network

The MANGO network began with seven red-line cameras with the field-of-view covering the majority of the continental United States. The red-line network was constructed between 2014 and 2016. The red-line network was able to reveal the latitudinal and longitudinal extent of medium- to large-scale TIDs and SAR arcs, as well as the intermixing of influences from magnetospheric sources and lower atmospheric drivers in mid-latitude ionosphere. These insights were possible due to the contiguous field-of-view provided by the red-line network. The red-line network regularly observed propagating waves connected to convective activity in the lower atmosphere. One of the primary sources of the convective activity was determined to be the Gulf of Mexico. However, the thermospheric conditions that made it possible for the convective activity to influence the ionospheric F-region were a complete unknown due to a lack of coincident measurements. To shed

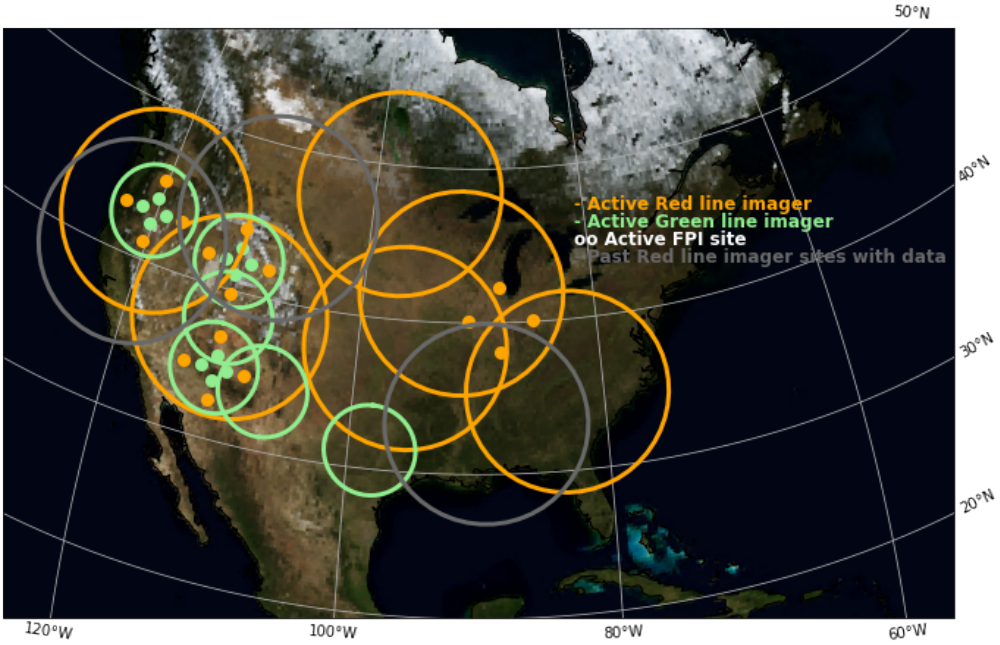

Figure 1. The current configuration of the MANGO network. Two of the sites in the western US have green line imagers and FPIs, while one site in Christmas Valley, Oregon has both red and green line imagers along with an FPI. The list of the sites is given in Table 1.

light on behavior of the lower thermosphere, we decided to augment the red-line network with a network of green-line imagers in addition to Fabry-Perot Interferometers observing both red and green line emissions. The completed network will ultimately have nine green-line imagers primarily in the western United States and eight red-line imagers. Installation of imagers in the US west/southwest leverages the relatively low-humidity regions with darker skies and enables observing the influence from the Gulf of Mexico.

3 Instruments

This section describes the two key instruments in the expanded MANGO network: the all-sky imagers (ASIs) and the Fabry-Perot Interferometers (FPIs).

Site name and code	Geographic Location	Instrument(s)				Operation time period
		Imager		FPI		
		Red	Green	Red	Green	
Christmas Valley, OR (CVO)	43.27° N -120.35° E	✓	✓	✓	✓	Dec 2021 – Now
Capitol Reef Field Station, UT (CFS)	38.15° N -111.18° E	✓	✓			May 2014 – Now
Bear Lake Observatory, UT (BLO)	41.6° N -111.6° E		✓	✓	✓	Aug 2021 – Now
Lowell Observatory, AZ (LOW)	35.20° N -111.66° E		✓	✓	✓	Aug 2021 – Now
Eastern Iowa Observatory, IA (EIO)	41.88° N -91.50° E	✓				Nov 2015 – Now
Madison, KS (MDK)	38.11° N -96.09° E	✓				July 2016 – Now
French Camp Observatory, MS (FCO)	33.29° N -89.38° E	✓				July 2016 – Mar 2018
Pisgah Astronomical Research Institute, NC (PAR)	35.20° N -82.87° E	✓				Sep 2016 – Jun 2018
Hat Creek Observatory, CA (HCO)	40.8° N -121.46° E	✓				Feb 2014 – Apr 2020
Bridger, MT (BMT)	45.34° N -108.91° E	✓				Nov 2015 – Dec 2017
Urbana Atmospheric Observatory, IL (UAO)	40.16° N -88.16° E			✓		2012 – Now
Magdalena Ridge Observatory, NM (MRO)	33.96° N -107.18° E		✓			Nov 2022 – Now
Big Dog Ranch, TX (BDR)	31.23° N -98.3° E		✓			Nov 2022 – Now
Martens Observatory, ND (MTO)	48.15° N -97.66° E	✓				Feb 2023 – Now

Figure 2. Current and historical sites in the MANGO network.

3.1 All-Sky Imagers

The MANGO all-sky imagers (ASIs) are based on the classic imager design used by geospace scientists for decades. The design is largely influenced by Mende et al. (1977) that was subsequently used in the THEMIS imagers and imagers built by the Boston University and deployed around the world [e.g., Martinis et al. (2003)]. The typical ASIs have been built as standalone systems with highly sensitive, actively cooled CCDs and often with multiple filters in a filter wheel. These systems have traditionally been expensive enough to only consider a standalone installation. The MANGO imager was designed with the idea of creating a monochromatic imaging network, and therefore has replaced all the custom-built parts required for multi-spectral imaging with commercial off-the-shelf components paired with an amateur astronomy camera, thus lowering the cost of each imager by a factor of 15 to 20. The first MANGO imager was calibrated (for integration time and the field-of-view) against the Boston University imager operating at the McDonald Observatory in Texas, USA. The results were used to set the exposure time for the red-line imager initially at 5 minutes.

The MANGO imager (Figure 3) has a fish-eye lens at the entrance aperture, followed by a double convex lens that nearly parallelizes the rays to go through the filter. The meniscus and the reimaging lens focus the rays on a 3/4-inch CCD used in Atik 414EX monochrome cameras. The filter for red-line is centered at 630.3nm with 2nm bandwidth, and for green-line is centered at 557.7nm with 1.6nm bandwidth. The narrow bandwidth helps with rejecting out-of-band emissions.

Most of the MANGO imagers are installed as autonomously operating stand-alone systems on rooftops of astronomical observatories and private homes. The rooftop installation utilizes non-penetrating roof-mounts that are secured to the roof with cinder blocks. The enclosure for the camera in dry, less-humid places has vents to enable airflow and temperature/humidity equivalence with the ambient atmosphere. This concept and enclosure design were first created in 2014 and have been used in subsequent enclosure designs for the MANGO systems. The three red-line imagers in high-humidity sites in North Carolina (PAR), Kansas (MDK), and Mississippi (FRC) have sealed enclosures with desiccant inside, but struggle with condensation during precipitation periods. The three green-line and one red-line imagers co-located with the FPIs (BLO, LOW, CVO) are internally roof-mounted with domes in the trailers. The red and green-line imagers at the CFS site in Utah are also roof-mounted in a building with domes.

There are some limitations of the MANGO systems: the imager assembly does not include a shutter, which means that dark background images are not acquired regularly and therefore are not part of the background subtraction. Since the CCD is always open to the light (though not powered), it accelerates degradation of the CCD. Any pixel degradation is not caught by the processing software due to the inability to background subtract every night. While this somewhat degrades the quality of the images the longer the camera is in the field, the camera itself is relatively inexpensive and easy to replace after a few years. Another limitation of the system with sealed enclosures is frequent condensation during winter months due to the temperature differential between outside and inside the enclosure. This problem often appears in the MANGO systems in eastern states (PAR, MDK) and those that are mounted with the trailer in somewhat humid regions (LOW, CVO).

3.2 Fabry-Perot Interferometers

Three imaging Fabry-Perot interferometers (FPIs) have been built and deployed to provide measurements of the neutral gas temperature and velocity (wind) at two altitudes in the mesosphere and thermosphere. This is accomplished by making high spectral resolution measurements of the 557.7- and 630.0-nm emissions, respectively. Each instrument is based on the successful MiniME design that has been deployed in Peru [e.g.,

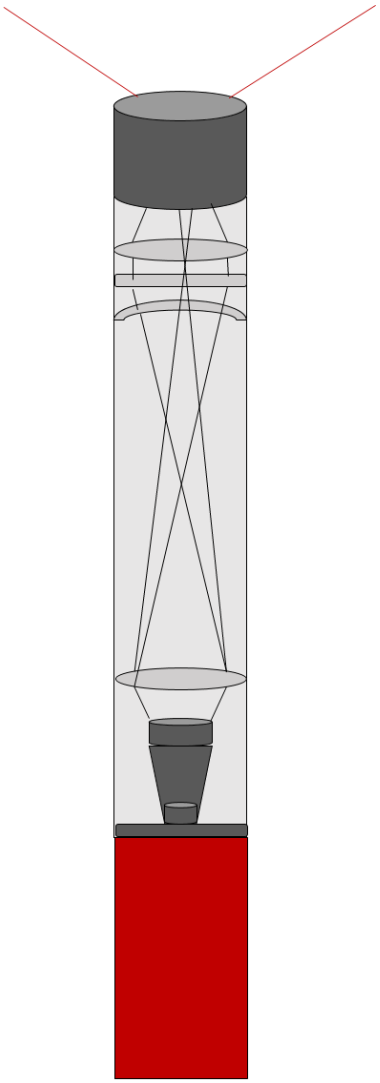

Figure 3. The MANGO imager schematic that images rays from 180^o field-of-view on to a 3/4-inch CCD through a series of lenses and the filter.

Meriwether et al. (2008)], Brazil [e.g., Makela et al. (2013)], North America [e.g., Makela (2012), Harding et al. (2019)], Morocco [e.g., Fisher et al. (2015), Malki et al. (2018), Loutfi et al. (2020)], Ethiopia [e.g., Tesema et al. (2017)], and South Africa [e.g., Ojo et al. (2022); Katamzi-Joseph et al. (2022)]. The simple, robust design is intended to accommodate long-term deployments with little need for on-site user intervention, making it an ideal companion to the MANGO imaging system.

Each system consists of a Sky-Scanner dual-axis mirror system, a filterwheel hosting two narrowband interference filters, a fixed-gap etalon, a reimaging lens, and a deep-cooled CCD, as shown in Figure 4. The Sky-Scanner was manufactured by KeoScientific and allows the field-of-view of the instrument to be steered to arbitrary locations in the sky, as needed to make wind estimates in the zonal and meridional directions. Control software is used to command the Sky-Scanner through user-defined sequences. The filterwheel was designed to accommodate up to four individually tiltable 86-mm diameter filters which are used to select the emissions of interest. The filter selection is controlled via a RaspberryPi, allowing the interleaving of measurements of the 557.7- and 630.0-nm emissions throughout the night. Bandwidths of 0.8 nm and 0.7 nm (full-width at half-max) are used to allow sufficient isolation of the 557.7- and 630.0-nm emissions, respectively, while still maintaining adequate signal intensity. The filter transmission is 55%. The narrower filter for the red-line filter is used to partially suppress the 629.8-nm contaminating OH emission. The fixed gap etalons, manufactured by IC Optical Systems, LTD, have an aperture of 70 mm, and a plate separation of 12.806 mm maintained by Zerodur spacers. The plates are coated to provide a 90% $\pm$ 4% (77% $\pm$ 1%) reflectivity at 557.7 nm (630.0 nm). The gap size of 12.806 mm was selected over the previously-used separation of 15.0 mm after an analysis of the potential for OH contamination, which in previous instrumentation was observed to pose a challenge to the analysis of the 630.0-nm emission during periods of low intensity. Finally, a reimaging lens with focal length of 300 mm focuses the incident light onto an iKon-M 934 CCD with 1024$\times$1024 pixels which can be cooled down to -70° C to minimize the effects of dark noise on the resultant images.

4 Data

This section describes data from both imagers and FPIs with details on data acquisition, transport and processing.

4.1 Imaging data

Image data are retrieved from the field sites using an automated data transport process. Once raw image files from remote sites arrive at the MANGO server, they must be processed to produce data suitable for scientific analysis. Raw images are stored as hdf5 files, each containing a single 2D array representing one camera image and accompanying metadata (i.e., site information, exposure time, image size, and camera parameters). Quick-look movies for each night are created from raw data after applying contrast adjustment and appropriate rotation angle.

Full-night processed data are provided in hdf5 files that each contain an image array which consists of all rotated, unwarped, contrast-adjusted images from a single night as well as time arrays for each image, coordinate arrays for each pixel, and various camera relevant parameters such as the CCD temperature. The rotation and unwarping procedures are very similar to those described in Garcia et al. (1997). First, a rotation and translation is applied to the image such that the camera field-of-view is centered with north upwards. Then a lens function is used to determine the correct elevation angle of each pixel. The lens function accounts for distortion due to the fish-eye lenses used by the imagers. The corrected elevation and azimuth angle can then be used to project the unwarped image to the assumed airglow altitude and calculate the geographic coordi-

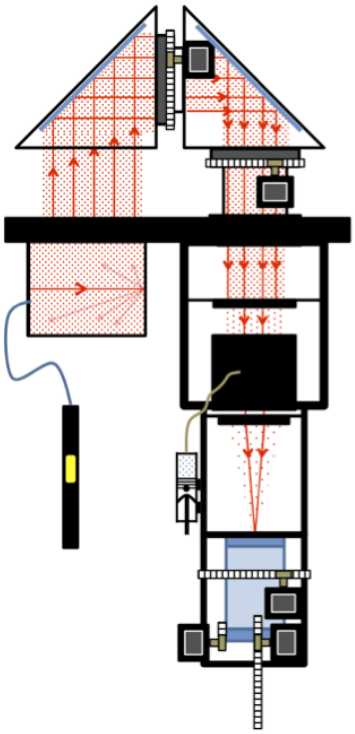

Figure 4. Schematic of the MiniME FPI system.

nates of each pixel. The rotation and translation coordinates, as well as the lens function coefficients can be found in advance by identifying stars with known positions in a cloud-free image and performing a nonlinear least squares fit to these parameters with the stars pixel locations. Figure 5 shows example unwarped images from the MANGO red line imagers.

4.2 FPI data

Custom software controls each FPI system and enables the observation of both the 557.7- and 630.0-nm emissions in arbitrary directions. It also allows for reference observations made to the zenith and towards a calibration chamber illuminated by a frequency-stabilized HeNe laser, which is used to account for instrument drift due to thermal fluctuations in the system. During typical operations, observations of both emissions are made between sunset and sunrise in the four cardinal directions and interleaved with observations towards zenith and the laser. Integration times are modified throughout the night to account for variations in the emission intensity, allowing shorter integration times in the beginning of the night when intensities tend to be brighter and longer integration times as the night progresses. A 30-second integration time minimum and 10-minute integration time maximum is enforced, but otherwise the integration time is dynamically modified so as to keep the expected measurement uncertainties around 5-10 m/s and 20-25 K. The distribution of integration times and uncertainties are shown for the first year of operations of the LOW FPI in Figure 6.

After being transferred from the remote sites, each night of data is automatically processed using a suite of Python routines as described in Makela et al. (2011) and Harding et al. (2014). This software transforms the two-dimensional interference pattern to a one-dimensional fringe pattern. Using data obtained by observing the frequency-stabilized

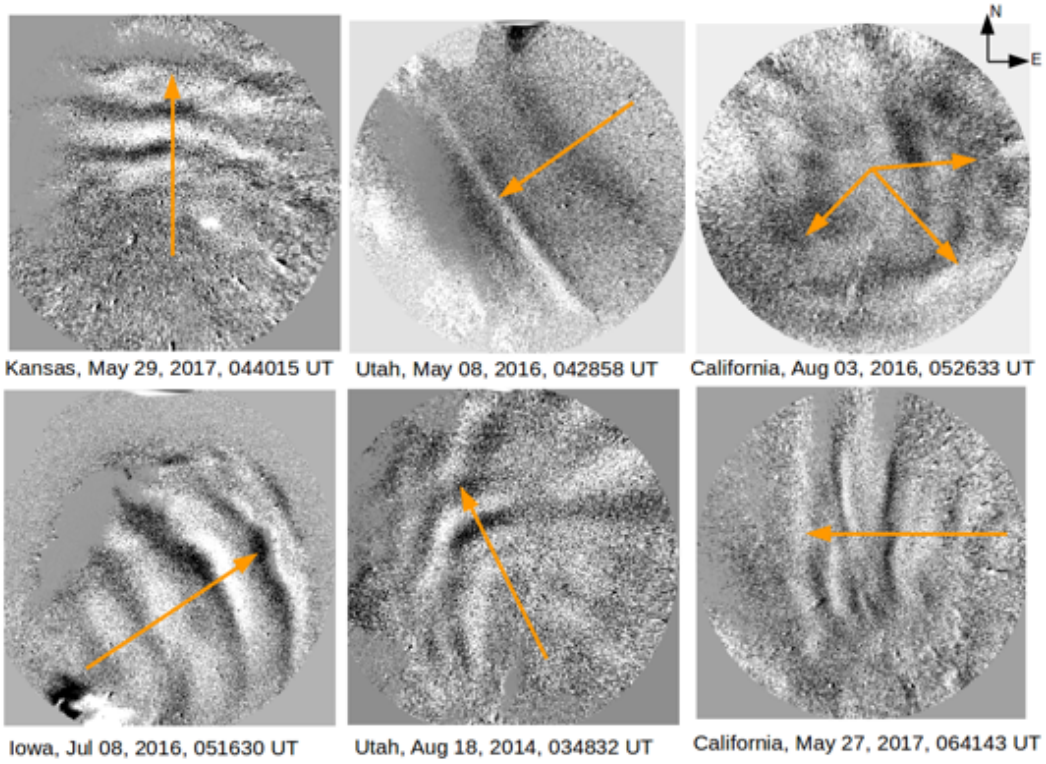

Figure 5. Example data from individual red line imagers from MANGO. Each example shows airglow depletions traveling in various directions.

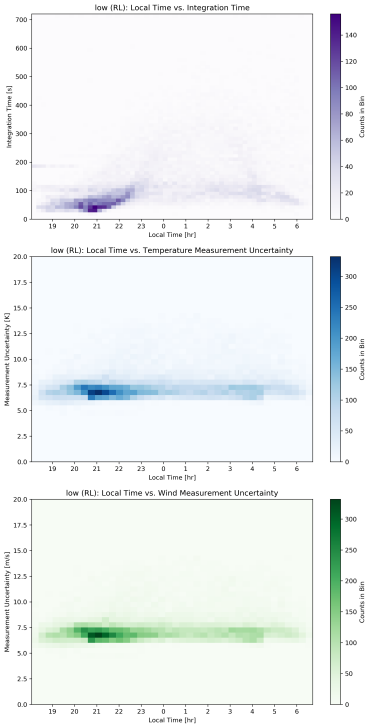

Figure 6. Statistics of measurements made of the neutral wind obtained by observing the 630.0-nm emission from LOW. (top) Number of observations in 15-minute bins of local time for a given integration time. Note more observations are made early in the evening with shorter integration times when the emission tends to be brighter. As the emission becomes dimmer throughout the night, the integration times increase. (middle) Number of observations in 15-minute bins of local time with a given wind uncertainty. (bottom) Same as the middle plot but for the estimated temperature uncertainty. Note that the uncertainties remain approximately constant throughout the night due to the use of the dynamic integration time settings.

HeNe laser, the instrument function parameters are then used in a non-linear regression of the one-dimensional fringe patterns obtained from looking at the sky, resulting in estimates of mesosphere/thermospheric winds and temperatures as well as statistical uncertainties in those estimates. Data are automatically transferred to the Madrigal database each day.

5 Key first results

5.1 Spatial correlations of lower and upper thermospheric wind

One of the primary goals of the MANGO FPI deployments was to establish longer baselines than in previous FPI networks such as the North American Thermosphere Ionosphere Observing Network (NATION) (Makela et al., 2014). A previous study by (Harding et al., 2019) used the NATION FPIs during 2013 to evaluate the the red-line thermospheric wind and quantify its similarity between nearby sites. That study decomposed the wind from each site into two parts: the "climate," the 60-day UT-dependent mean, and the "weather," the residual from that mean. Pairs of sites (baselines of 300–800 km) were compared and cross-correlated. It was found that the cross-correlation of the weather dropped quickly with baseline distance, reaching ∼0.4 at 800 km. From that study it was impossible to determine the decorrelation distance (the baseline at which the cross-correlation drops to e^{-1}), but extrapolating the trend suggested a value of about 1,000 km.

In this section, we extend the analysis of (Harding et al., 2019) in two ways: to the longer baselines spanned by the MANGO FPIs (750–2,700 km, when combined with the long-running FPI at UAO), and to the lower thermospheric (green-line) wind. We use available data at the time of writing for which all four FPI sites were operational, spanning 13 months (1 Dec 2021 to 31 Dec 2022) and follow the analysis process described by (Harding et al., 2019). Briefly, the line-of-sight winds from each instrument are collected into 30-minute bins, and the average zonal wind, meridional wind, and Doppler offset are computed in the least-squares sense, assuming the average vertical wind is zero. Only geomagnetically quiet periods are analyzed; timestamps are omitted if the maximum Kp in the previous 24 hours was greater than 3.0. This step removes about half of the data. Quality control is performed according to Section 3.2 of (Harding et al., 2019) except for two details: (1) the temperature threshold was reduced from 150 K to 50 K for the green-line analysis to account for the normally colder temperatures in the lower thermosphere, and (2) the cloud detector threshold (i.e., the value of the infrared sky temperature minus the ambient temperature above which it is considered cloudy) was raised from -22°C to -12°C because for an unknown reason the cloud detector at some sites often gives readings above -22°C even when it is clear. All other quality control steps are identical to (Harding et al., 2019) (e.g., OH contamination mitigation, removal of bad fits, and identification of large background emission such as moonlight).

Figure 7 shows wind data for 60 days surrounding 19 May 2022 at the LOW site, a representative example. Red-line (top left) and green-line (top right) data are analyzed separately. Individual nights of data are shown in thin red or green lines, and the 60-day mean is shown in a thick red or green line. Here only the zonal wind component is shown. The mean is compared to the prediction by the empirical Horizontal Wind Model 2014 (Drob et al., 2015) (thick black line). The data and model compare reasonably well in the mean sense, although in the red line, some higher-order tidal features seem to be more apparent in the data than in the model, which has been observed before (e.g., Ojo et al., 2022).

A striking feature is the variability about the mean behavior, i.e., the weather, the magnitude of which is commensurate with the magnitude of climactic variations. The bottom panels of Figure 7 show the difference between the daily data and the 60-day mean. We define this component as the weather, which is further analyzed as in Harding et al.

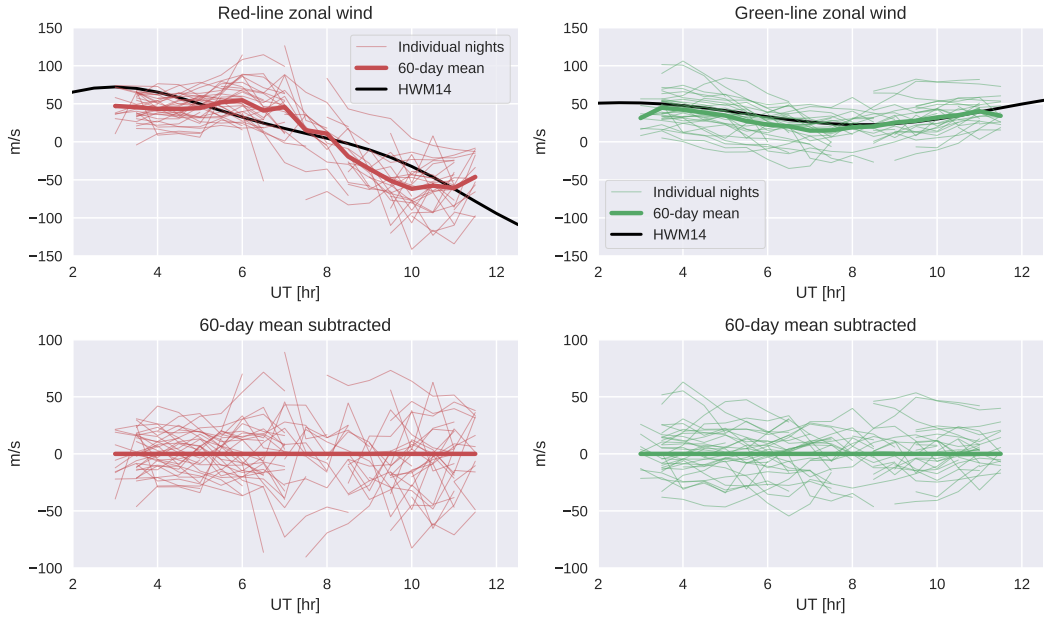

Figure 7. Example FPI zonal wind data from the LOW site for 60 days centered 19 May 2022. Red-line winds (∼250 km altitude) are on the left and green-line winds (∼98 km altitude) are on the right. Top panels show individual nights of data (thin red/green lines) with the 60-day UT-dependent mean (thick red/green lines) and HWM14 (thick black line). Bottom panels show the "weather" component, the residual from the 60-day mean.

(2019). By eye, this variation appears random – not related to slow seasonal changes or long-period planetary wave forcing, but rather highly variable from one day to the next, in both the lower and upper thermosphere. This is perhaps related to the irregular or "stochastic" component of variability discussed by Liu (2016).

To perform a preliminary analysis of this variability, we compute its spatial correlation in Figure 8. For each pair of FPIs, the cross-correlation of the weather is computed for the red line (left panel) and green line (right panel). More baselines are available for the red-line because the UAO FPI (which only has a red-line filter) can be used. Analogous results from the NATION FPIs (taken from Figure 4 of Harding et al. (2019)) are shown as white circles and squares (red-line only).

In the red line, the MANGO spatial correlations are mostly consistent with the results from NATION, especially for the meridional winds (circles), with correlations near 0.4 at baselines of 750 km. The MANGO zonal wind correlations at ∼750 km span 0.4–0.75, while the NATION correlations were 0.4–0.5.

Overall, the red-line correlations from MANGO are higher than would be predicted from a simple extrapolation of the NATION results. There are multiple possibilities for this. This might be physical: A sharp drop in the correlation function from 0 to ∼1,000 km is consistent with variability introduced by gravity waves, while the flattening of the correlation function at longer baselines is consistent with variability introduced by large-scale features such as tides and planetary waves. Other possibilities include sampling and data artifacts. For example, NATION data were taken in the solar maximum of 2013, while MANGO data shown here are from 2021, rising out of solar minimum. In solar maximum, one expects more aurorally generated GWs, and in solar minimum one expects greater vertical penetration of tides from the lower atmosphere. NATION baselines were

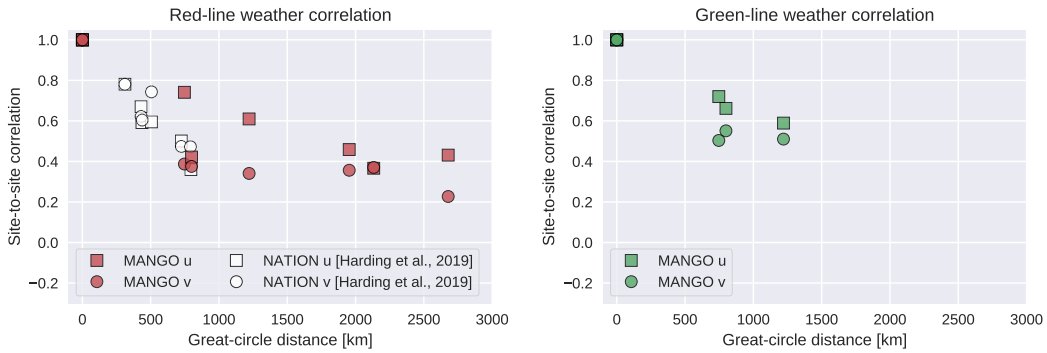

Figure 8. Cross-correlations of the weather between all pairs of FPIs in MANGO (red/green symbols) for both the zonal (u, red squares) and meridional (v, red circles) wind. Analogous results from NATION data from Harding et al. (2019) are also shown (white symbols).

in the eastern US, while the MANGO baselines span western-central US. Gravity wave activity from orographic and convective forcing may be different in these locations. North-south and east-west baselines may show different behavior due to orientation of GWs and/or latitudinal dependence of tides. However, no obvious dependence on spatial orientation was found to resolve the discrepancies shown. Another possible factor is that each correlation is computed using a slightly different set of dates, since the set of dates when all sites are clear and operating is insufficient for good statistics. Finally, quality control issues (e.g., cloud detection) are a possible contributing factor. Ongoing work is investigating the utility of the co-located MANGO imagers for improved automatic cloud detection. These are just a few possibilities which will be investigated in future work. Many of these issues could be mitigated with a longer-term, larger, identically operated and processed network of FPIs.

Regarding the green-line results (Figure 8, right panel), the 750–1,250-km correlations are 0.5–0.7. Our initial expectation was that green-line correlations would be larger than red-line correlations. By visual inspection, individual nights of green-line wind data are usually smoother temporally than red-line data, suggesting a dominance of long-period waves likes tides, which have long correlation lengths. Furthermore, aurorally generated gravity waves do not penetrate down to the green-line layer (95-100 km), while they can dominate at the red-line layer (250 km), and many of the tides in the mesosphere and lower thermosphere do not penetrate to the upper thermosphere. Nevertheless, the MANGO data indicate that green-line decorrelation is not significantly different than red-line decorrelation over spatial scales of 750–1,250 km. Comparisons to first-principles models capable of capturing day-to-day variability from the lower atmosphere (e.g., WACCM-X, GAIA, WAM-IPE) will be able to provide further insight.

5.2 Simultaneous observations of green-line gravity waves and winds

An example MANGO network mosaic image of the green-line emission obtained on May 25, 2022 is shown in Figure 9. The mosaics are created by first temporally filtering the imaging data from each site using a 13-tap finite impulse response (FIR) filter with a low cutoff period of 2 minutes and high cutoff period of 20 minutes. On this night, green-line data from four sites (CVO, BLO, CFS, and LOW) are available. The images are then projected onto an assumed emission layer of 95 km. At each time, the green-line neutral winds obtained from the collocated FPI systems at the CVO and BLO sites are found and plotted as a vector (the LOW FPI experienced technical difficulties on this night and did not collect data). The plots to the right show the time history of

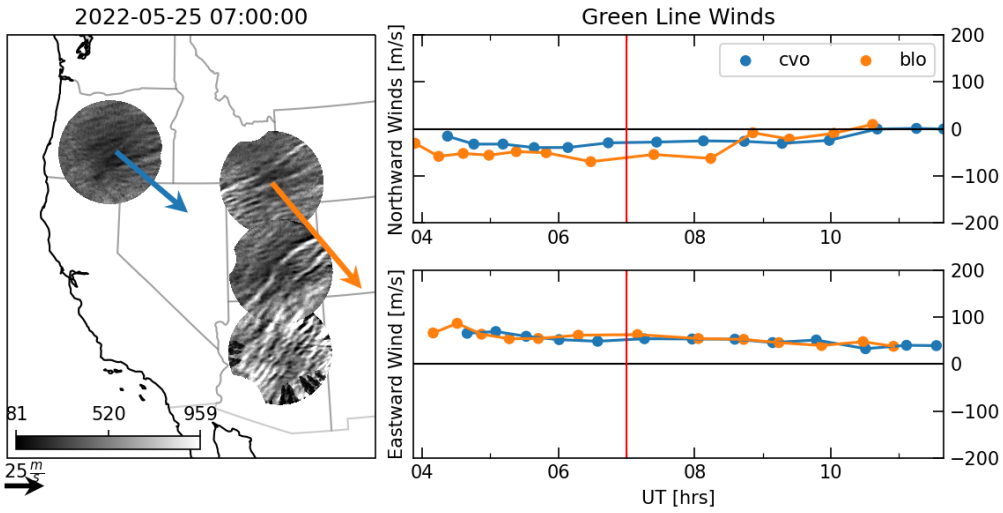

Figure 9. Example MANGO network mosaic image obtained at 0700 UT on May 25, 2022. (left) images of the green-line emission obtained from four MANGO sites. The green arrows show the measured green-line neutral winds. (right) Cardinal components of the neutral winds measured from the two sites shown as vectors in the left plot. The vertical line indicates the time shown in the image to the left. A full animation of the results on this night is provided in the supplemental material.

the neutral winds, broken out into the (top) northward and (bottom) eastward components. The vertical red line on these plots indicates the time corresponding to the images in the left panel. Although the altitude of the green-line layer is uncertain, the retrieved wind and wave signatures are derived from the same emission, and thus arise from the same altitude and subject to the same vertical averaging.

In this particular example, a variety of wave structures are seen over the western United States. Encouragingly, the wave fronts seen in the northern half of the LOW imager and the southern half of the CFS imager are coherent at the boundaries between the two imagers, indicating that both the temporal filtering and spatial projection steps are capturing the same wave features from the two different sites. This is apparent in the animation of all of the images, which is provided in the supplemental material. The animation clearly shows the propagation of the waves towards the northwest on this night and their coherence as they pass through the fields-of-view of each imaging system.

It is interesting to note that the wave features are propagating against the background neutral wind, consistent with wave filtering theory which indicates that atmospheric gravity waves will dissipate into the background fluid when propagating in the same direction and speed as the background fluid [e.g., Cowling et al. (1971). On this night, the sustained wave activity propagating *against* the background neutral wind indicates that the wave energy could penetrate upwards and dissipate at a higher altitude.

Visual inspection of multiple nights suggests that the wind and wave field can be much more variable than the example presented. Future work will study the relationship between the wave propagation characteristics (i.e., orientation and speed) in relation to the variable neutral wind. Additionally, a filtering technique, based on the work presented in Grawe and Makela (2017), will be employed to quantitatively study the orientation, wavelength, and velocity of the waves observed in the green-line images.

5.3 Geomagnetic storm impact on red-line airglow

The red-line cameras in the MANGO network extend from sub-auroral to mid-latitudes. During geomagnetically active conditions, many sub-auroral imagers observe diffuse aurora along with sub-auroral red (SAR), STEVE Martinis et al. (2021), imagers at all latitudes observe Large-Scale TIDs (LSTIDs) Lyons et al. (2019), and imagers at low-latitudes have observed enhanced airglow associated with storm-time density enhancement. Here we describe one geomagnetically active event that had significant impact at all latitudes observed by the MANGO red-line imagers.

A slow-moving coronal mass ejection (CME) from the sun arrived at earth at 1500 UT on May 27, 2017, which sparked a Kp=7 storm on May 28. As the imagers came online starting in the east coast starting 0400 UT, we see southwestward moving features commonly associated with electrified TIDs (Shiokawa et al., 2003). However, the same features start changing the tilt and become east-west aligned around 0730 UT, with appearance of diffuse aurora in the imagers in Kansas and Montana and enhanced airglow in the imagers in Utah and California. The electron density and field-aligned currents data from SWARM satellite show that the mid-latitude trough was at 40^oN latitude during this time with significantly enhanced densities at equatorial and low/mid latitudes, effectively squeezing the mid-latitudes. Figure 10 shows this transition. Jonah et al. (2018) examined this event using the GNSS TEC dataset and mainly found the TIDs of various types. However, the data presented here shows the event to be more complex in nature. We present this example here to show that complex events require integration of multiple types of observations to understand the underlying physics, and that comprehensive data analysis studies are now possible with the large MANGO dataset.

5.4 Other phenomena Observed in MANGO data

Apart from the more readily explainable phenomena like gravity waves/TIDs from various sources, aurora, SAR arcs, the MANGO network also observes interesting phenomena, which require in-depth analysis. These include secondary waves from the Hunga Tonga volcanic eruption Inchin et al. (2023), STEVE Martinis et al. (2021), and a few phenomena shown in Figure 11. Specifically, the red-line imagers have observed airglow depletion appearing as thin 'fingers' that advect without changing shape or developing along the length of the depletion. Similarly 'swirling' airglow enhancement has also been observed. Another unexplained, but regularly occurring phenomenon is poleward moving gravity waves/TIDs during geomagnetically active conditions. The phenomena outlined here are examples that require separate investigations.

6 Summary and future plans

In this paper, we have described the MANGO network of red and green line imagers and FPIs that are deployed in the continental United States to observe nightime airglow emissions in OI 557.7-nm and OI 630.0-nm wavelengths and derive properties of observed waves and winds. The completed network will have 7 red-line and 9 green-line imagers plus 4 FPIs measuring both red and green line winds. The imager data along with combined green line images and winds movies from this network are continuously streaming and being made available in near-real time ($<$ 24 hours delay) through a web-interface at `mangonetwork.org`. The goal of the NSF DASI program was to establish such a network of distributed instruments that can operate with low maintenance and continually produce data for both geospace science and space weather needs. The MANGO deployment has realized this capability for thermospheric winds and waves, and operations will continue provided availability of funds for its modest operating and maintenance costs.

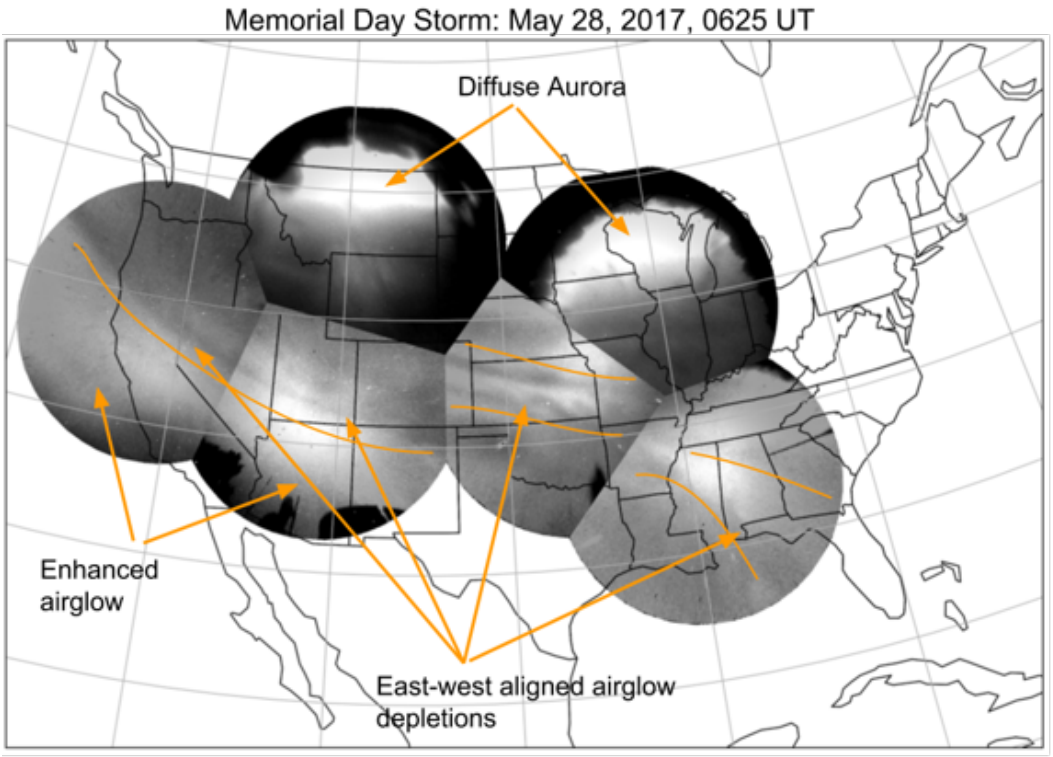

Figure 10. The MANGO red line mosaic image obtained on 2017-05-28 at 0635-0636 UTC showing bright aurora in northern imagers, east-west spanning airglow depletion in four southern imagers and bright airglow enhancement south of the depletion in the two westernmost imagers (HCO and CFS sites).

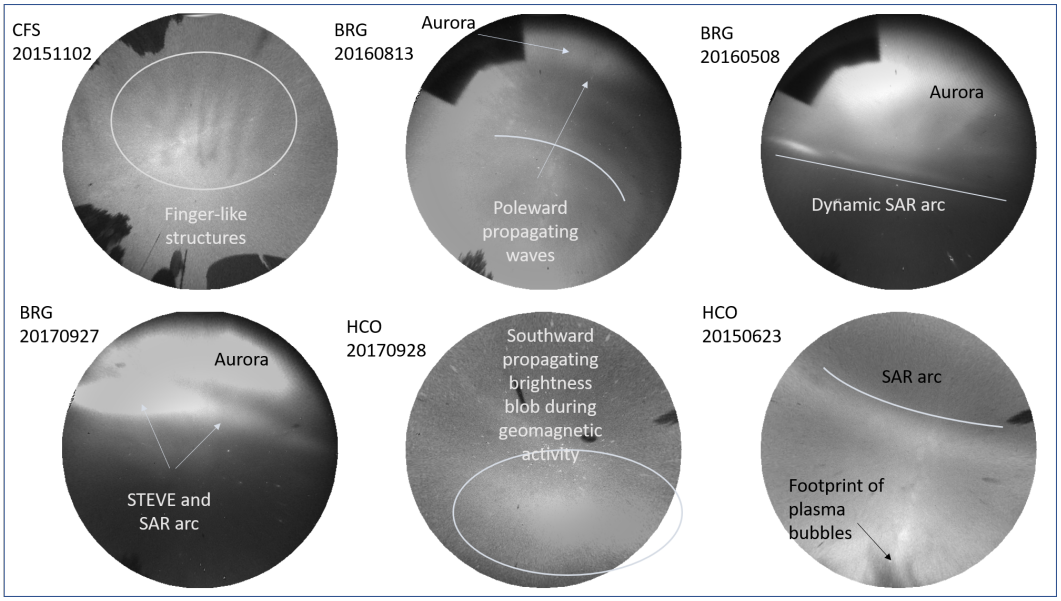

Figure 11. Some examples of interesting phenomena observed requiring further investigations are a) frozen finger-like airglow depletions expanding north to south and propagating westward b) poleward propagating waves during geomagnetic activity c) dynamic SAR arc with variable brightness d) colocated STEVE and SAR arc e) southward propagating brightness blobs during strong geomagnetic activity, and f) footprints of equatorial plasma bubbles observed along with SAR arc during extreme geomagnetic activity.

7 Open Research

Software for both the data transport system that retrieves data from the MANGO images and the processing pipeline are available at `https://github.com/mangonetwork`. All raw data processing code is written in Python and publicly available as open source software under GNU GPLv3 (`https://github.com/mangonetwork/raw-image-processing`). These are all licensed under GNU General Public License v3.0. Raw MANGO imaging data are available at `https://data.mangonetwork.org/data/transport/mango/archive/`. QuickLook movies are available online for viewing from `https://mangonetwork.org`. Processed FPI data (winds, emission rates, uncertainties, quality flags, etc.) are publicly available from the Madrigal database (http://cedar.openmadrigal.org/)

Acknowledgments

The imaging and FPI data are obtained through the MANGO network operated by SRI and University of Illinois, respectively. Work at the University of California, Berkeley is supported through NSF award AGS-1933077, at SRI International is supported through NSF award AGS-1933013, and at the University of Illinois is supported through NSF award AGS-1932953. The initial MANGO red-line imagers were deployed through NSF award AGS-1452357. We would like to acknowledge the help of Jeffrey Baumgardner and Robert Marshall in developing the first MANGO imager. We thank John Kendall, Geoff Mangus and Mike Greffen for their assistance with developing the MANGO imager enclosures. We thank Steven Chen and Ashton Reimer for their help with setting up first MANGO data servers. We would like to thank the operators and facilitators that made MANGO site installations possible. These include, Joseph Ceradini and Michael Hague at the Capitol Reef Field Station/Utah Valley University (CFS), Bert Kraft and

Cynthia Tripp (BRG), Kim Kingery and Dacia and Warren Brandt (MDK), Palisades-Dows Observatory and John Leeson (EIO), Edwin Faughn (FRC), Simon Shepherd and Donald Severns (CVO), Mike Taylor and Donald Rice (BLO), Kyler Kuehn and Jake Tiegs (LOW), Michelle Creech-Eakman and Chris Salcido at the Magdalena Ridge Observatory (MRO), Don Hampton and Steve Schmidt (BDR), and Tim Young at the Martens Observatory (MTO).

References

Cowling, D. H., Webb, H. D., & Yeh, K. C. (1971). Group rays of internal gravity waves in a wind-stratified atmosphere. *Journal of Geophysical Research (1896-1977)*, *76*(1), 213-220. Retrieved from https://agupubs.onlinelibrary.wiley.com/doi/abs/10.1029/JA076i001p00213 doi: https://doi.org/10.1029/JA076i001p00213

Drob, D. P., Emmert, J. T., Meriwether, J. W., Makela, J. J., Doornbos, E., Conde, M. G., ... Klenzing, J. H. (2015). An update to the Horizontal Wind Model (HWM): The quiet time thermosphere. *Earth and Space Science*, *2*(7), 301–319. Retrieved from http://doi.wiley.com/10.1002/2014EA000089 doi: 10.1002/2014EA000089

Fisher, D. J., Makela, J. J., Meriwether, J. W., Buriti, R. A., Benkhaldoun, Z., Kaab, M., & Lagheryeb, A. (2015). Climatologies of nighttime thermospheric winds and temperatures from Fabry-Perot interferometer measurements: From solar minimum to solar maximum. *Journal of Geophysical Research A: Space Physics*, *120*(8), 6679–6693. doi: 10.1002/2015JA021170

Garcia, F. J., Kelley, M. C., Makela, J. J., & Huang, C.-S. (2000). Airglow observations of mesoscale low-velocity traveling ionospheric disturbances at midlatitudes. *Journal of Geophysical Research*, *105*(A8), 18407. Retrieved from http://doi.wiley.com/10.1029/1999JA000305 doi: 10.1029/1999JA000305

Garcia, F. J., Taylor, M. J., & Kelley, M. C. (1997, Oct). Two-dimensional spectral analysis of mesospheric airglow image data. *Appl. Opt.*, *36*(29), 7374–7385. Retrieved from https://opg.optica.org/ao/abstract.cfm?URI=ao-36-29-7374 doi: 10.1364/AO.36.007374

Grawe, M. A., & Makela, J. J. (2017). Observation of tsunami-generated ionospheric signatures over hawaii caused by the 16 september 2015 illapel earthquake. *Journal of Geophysical Research: Space Physics*, *122*(1), 1128-1136. Retrieved from https://agupubs.onlinelibrary.wiley.com/doi/abs/10.1002/2016JA023228 doi: https://doi.org/10.1002/2016JA023228

Harding, B. J., Gehrels, T. W., & Makela, J. J. (2014). Nonlinear regression method for estimating neutral wind and temperature from Fabry-Perot interferometer data. *Applied Optics*, *53*(4), 666. Retrieved from http://www.opticsinfobase.org/abstract.cfm?URI=ao-53-4-666 doi: 10.1364/AO.53.000666

Harding, B. J., Makela, J. J., & Meriwether, J. W. (2015). Estimation of mesoscale thermospheric wind structure using a network of interferometers. *Journal of Geophysical Research: Space Physics*, *120*(5), 3928–3940. Retrieved from http://doi.wiley.com/10.1002/2015JA021025 doi: 10.1002/2015JA021025

Harding, B. J., Ridley, A. J., & Makela, J. J. (2019). Thermospheric weather as observed by ground-based fpis and modeled by gitm. *Journal of Geophysical Research: Space Physics*, *124*(2), 1307-1316. Retrieved from https://agupubs.onlinelibrary.wiley.com/doi/abs/10.1029/2018JA026032 doi: https://doi.org/10.1029/2018JA026032

Inchin, P. A., Bhatt, A., Cummer, S., Harding, B., J., M. J., Sabatini, R., & B., S. J. (2023). *Multi-layer evolution of acoustic-gravity waves over continental*

united states after the 2022 hunga volcano eruption. (Under Review)

Jonah, O. F., Coster, A., Zhang, S., Goncharenko, L., Erickson, P. J., de Paula, E. R., & Kherani, E. A. (2018). Tid observations and source analysis during the 2017 memorial day weekend geomagnetic storm over north america. *Journal of Geophysical Research: Space Physics*, *123*(10), 8749-8765. Retrieved from https://agupubs.onlinelibrary.wiley.com/doi/abs/10.1029/2018JA025367 doi: https://doi.org/10.1029/2018JA025367

Katamzi-Joseph, Z. T., Grawe, M. A., Makela, J. J., Habarulema, J. B., Martinis, C., & Baumgardner, J. (2022). First results on characteristics of nighttime mstids observed over south africa: Influence of thermospheric wind and sporadic e. *Journal of Geophysical Research: Space Physics*, *127*(11), e2022JA030375. Retrieved from https://agupubs.onlinelibrary.wiley.com/doi/abs/10.1029/2022JA030375 (e2022JA030375 2022JA030375) doi: https://doi.org/10.1029/2022JA030375

Kubota, M., Fukunishi, H., & Okano, S. (2001). Characteristics of medium- and large-scale tids over japan derived from oi 630-nm nightglow observation. *Earth Planets and Space*, *53*, 741-751. doi: https://doi.org/10.1186/BF03352402

Liu, H. L. (2016). Variability and predictability of the space environment as related to lower atmosphere forcing. *Space Weather*, *14*(9), 634–658. doi: 10.1002/2016SW001450

Loutfi, A., Bounhir, A., Pitout, F., Benkhaldoun, Z., & Makela, J. J. (2020). Thermospheric Neutral Winds Above the Oukaimeden Observatory: Effects of Geomagnetic Activity. *Journal of Geophysical Research: Space Physics*, *125*(7), 1–17. doi: 10.1029/2019JA027383

Lyons, L. R., Nishimura, Y., Zhang, S. R., Coster, A. J., Bhatt, A., Kendall, E., & Deng, Y. (2019). Identification of Auroral Zone Activity Driving Large-Scale Traveling Ionospheric Disturbances. *Journal of Geophysical Research: Space Physics*, *124*(1), 700–714. doi: 10.1029/2018JA025980

Makela, J. J. (2012). *ISS Airglow Proposal* (No. April).

Makela, J. J., Fisher, D. J., Meriwether, J. W., Buriti, R. A., & Medeiros, A. F. (2013, 10). Near-continual ground-based nighttime observations of thermospheric neutral winds and temperatures over equatorial Brazil from 2009 to 2012. *Journal of Atmospheric and Solar-Terrestrial Physics*, *103*, 94–102. Retrieved from http://linkinghub.elsevier.com/retrieve/pii/S1364682612002957 doi: 10.1016/j.jastp.2012.11.019

Makela, J. J., Harding, B. J., Meriwether, J. W., Mesquita, R., Sanders, S., Ridley, A. J., ... Martinis, C. R. (2014). Storm time response of the midlatitude thermosphere: Observations from a network of Fabry-Perot interferometers. *Journal of Geophysical Research: Space Physics*, *119*(8), 6758–6773. Retrieved from http://doi.wiley.com/10.1002/2014JA019832 doi: 10.1002/2014JA019832

Makela, J. J., Meriwether, J. W., Huang, Y., & Sherwood, P. J. (2011). Simulation and analysis of a multi-order imaging Fabry-Perot interferometer for the study of thermospheric winds and temperatures. *Applied Optics*, *50*(22), 4403–16. Retrieved from http://www.ncbi.nlm.nih.gov/pubmed/21833117

Makela, J. J., Meriwether, J. W., Ridley, A. J., Ciocca, M., & Castellez, M. W. (2012). Large-Scale Measurements of Thermospheric Dynamics with a Multisite Fabry-Perot Interferometer Network: Overview of Plans and Results from Midlatitude Measurements. *International Journal of Geophysics*, *2012*. doi: 10.1155/2012/872140

Malki, K., Bounhir, A., Benkhaldoun, Z., Makela, J. J., Vilmer, N., Fisher, D. J., ... Lazrek, M. (2018, 7). Ionospheric and thermospheric response to the 27–28 February 2014 geomagnetic storm over north Africa. *Annales Geophysicae*, *36*(4), 987–998. Retrieved from https://www.ann-geophys.net/36/987/

2018/ doi: 10.5194/angeo-36-987-2018

Martinis, C., Baumgardner, J., Wroten, J., & Mendillo, M. (2010). Seasonal dependence of mstids obtained from 630.0 nm airglow imaging at arecibo. *Geophysical Research Letters*, *37*(11). Retrieved from https://agupubs.onlinelibrary.wiley.com/doi/abs/10.1029/2010GL043569 doi: https://doi.org/10.1029/2010GL043569

Martinis, C., Eccles, J. V., Baumgardner, J., Manzano, J., & Mendillo, M. (2003). Latitude dependence of zonal plasma drifts obtained from dual-site airglow observations. *Journal of Geophysical Research: Space Physics*, *108*(A3). Retrieved from https://agupubs.onlinelibrary.wiley.com/doi/abs/10.1029/2002JA009462 doi: https://doi.org/10.1029/2002JA009462

Martinis, C., Nishimura, Y., Wroten, J., Bhatt, A., Dyer, A., Baumgardner, J., & Gallardo-Lacourt, B. (2021). First simultaneous observation of STEVE and SAR arc combiningdata from citizen scientists, 630.0 nm all-sky images, and satellites. *Geophysical Research Letters*, 1–9. doi: 10.1029/2020gl092169

Mende, S. B., Angelopoulos, V., Frey, H. U., Harris, S., Donovan, E., Jackel, B., ... Mann, I. (2007). Determination of substorm onset timing and location using the themis ground based observatories. *Geophysical Research Letters*, *34*(17). Retrieved from https://agupubs.onlinelibrary.wiley.com/doi/abs/10.1029/2007GL030850 doi: https://doi.org/10.1029/2007GL030850

Mende, S. B., Eather, R. H., & Aamodt, E. K. (1977, 6). Instrument for the monochromatic observation of all sky auroral images. *Applied optics*, *16*(6), 1691–700. Retrieved from http://www.ncbi.nlm.nih.gov/pubmed/20168774

Mendillo, M., Baumgardner, J., Nottingham, D., Aarons, J., Reinisch, B., Scali, J., & Kelley, M. (1997). Investigations of thermospheric-ionospheric dynamics with 6300-Å images from the arecibo observatory. *Journal of Geophysical Research: Space Physics*, *102*(A4), 7331-7343. Retrieved from https://agupubs.onlinelibrary.wiley.com/doi/abs/10.1029/96JA02786 doi: https://doi.org/10.1029/96JA02786

Meriwether, J. W., Faivre, M., Fesen, C., Sherwood, P., & Veliz, O. (2008, 3). New results on equatorial thermospheric winds and the midnight temperature maximum. *Annales Geophysicae*, *26*(3), 447–466. Retrieved from http://adsabs.harvard.edu/abs/2008AnGeo..26..447Mhttp://www.ann-geophys.net/26/447/2008/ doi: 10.5194/angeo-26-447-2008

Navarro, L., & Fejer, B. (2019, 10). Storm-Time Thermospheric Winds Over Peru. *Journal of Geophysical Research: Space Physics*, 2019JA027256. Retrieved from https://onlinelibrary.wiley.com/doi/abs/10.1029/2019JA027256 doi: 10.1029/2019JA027256

Nishitani, N., Ruohoniemi, J. M., Lester, M., Baker, J. B. H., Koustov, A. V., Shepherd, S. G., ... Kikuchi, T. (2019). Review of the accomplishments of mid-latitude Super Dual Auroral Radar Network (SuperDARN) HF radars. *Progress in Earth and Planetary Science*, *6*(1). doi: 10.1186/s40645-019-0270-5

Ojo, T. T., Katamzi-Joseph, Z. T., Chu, K. T., Grawe, M. A., & Makela, J. J. (2022). A climatology of the nighttime thermospheric winds over Sutherland, South Africa. *Advances in Space Research*, *69*(1). Retrieved from https://doi.org/10.1016/j.asr.2021.10.015 doi: 10.1016/j.asr.2021.10.015

Shiokawa, K., Otsuka, Y., Ihara, C., Ogawa, T., & Rich, F. J. (2003). Ground and satellite observations of nighttime medium-scale traveling ionospheric disturbance at midlatitude. *Journal of Geophysical Research: Space Physics*, *108*(A4). Retrieved from https://agupubs.onlinelibrary.wiley.com/doi/abs/10.1029/2002JA009639 doi: https://doi.org/10.1029/2002JA009639

Taylor, M. (1997, 1). A review of advances in imaging techniques for measuring short period gravity waves in the mesosphere and lower thermosphere. *Advances in Space Research*, *19*(4), 667–676. Retrieved from

http://linkinghub.elsevier.com/retrieve/pii/S0273117797001610 doi: 10.1016/S0273-1177(97)00161-0

Tesema, F., Mesquita, R., Meriwether, J., Damtie, B., Nigussie, M., Makela, J., ... Sanders, S. (2017, 3). New results on equatorial thermospheric winds and temperatures from Ethiopia, Africa. *Annales Geophysicae*, *35*(2), 333–344. Retrieved from https://www.ann-geophys.net/35/333/2017/ doi: 10.5194/angeo-35-333-2017

Tsugawa, T., Otsuka, Y., Coster, A. J., & Saito, A. (2007). Medium-scale traveling ionospheric disturbances detected with dense and wide tec maps over north america. *Geophysical Research Letters*, *34*(22). Retrieved from https://agupubs.onlinelibrary.wiley.com/doi/abs/10.1029/2007GL031663 doi: https://doi.org/10.1029/2007GL031663